University of Birmingham

Convective and absolute instability of viscoelastic liquid jets in the presence of gravity

Alhushaybari, Abdullah; Uddin, Jamal

[Link to publication on Research at Birmingham portal](#)

Convective and absolute instability of viscoelastic liquid jets in the presence of gravity

A. Alhushaybari (iD), and J. Uddin

View Online   Export Citation   CrossMark

Convective and absolute instability of viscoelastic liquid jets in the presence of gravity

A. Alhushaybari[a]) (ID) and J. Uddin[b])

AFFILIATIONS

School of Mathematics, The University of Birmingham, Birmingham B15 2TT, United Kingdom

[a)]**Author to whom correspondence should be addressed:** aba574@student.bham.ac.uk
[b)]**Electronic mail:** j.uddin@bham.ac.uk

ABSTRACT

The convective and absolute instability of a viscoelastic liquid jet falling under gravity is examined for axisymmetrical disturbances. We use the upper-convected Maxwell model to provide a mathematical description of the dynamics of a viscoelastic liquid jet. An asymptotic approach, based on the slenderness of the jet, is used to obtain the steady state solutions. By considering traveling wave modes, we derive a dispersion relation relating the frequency to the wavenumber of disturbances which is then solved numerically using the Newton-Raphson method. We show the effect of changing a number of dimensionless parameters, including the Froude number, on convective and absolute instability. In this work, we use a mapping technique developed by Kupfer, Bers, and Ram ["The cusp map in the complex-frequency plane for absolute instabilities," Phys. Fluids **30**, 3075–3082 (1987)] to find the cusp point in the complex frequency plane and its corresponding saddle point (the pinch point) in the complex wavenumber plane for absolute instability. The convective/absolute instability boundary is identified for various parameter regimes.

Published under license by AIP Publishing. https://doi.org/10.1063/1.5089242

I. INTRODUCTION

The instability, and subsequent disintegration, of a column of fluid is of interest in a wide variety of growing applications (such as ink jet printing,[2] nanofiber,[3] needle-free injection,[4] coating, and even diesel engine technology[5]). Despite over 200 years of scientific scrutiny, the instability of a liquid jet remains an active area of study for many researchers from a wide range of scientific disciplines. A jet can be defined as a stream that is propelled into a medium via an opening such as a nozzle. In general, liquid jets are unstable in nature and ultimately break up into droplets.[6] The primary mechanism of this breakup is the Rayleigh-Plateau instability which is identified by the growth of disturbances that are either absolutely or convectively unstable. Convective instability grows in amplitude as it is swept along by the flow, whereas absolute instability occurs at fixed spatial locations.[7] Furthermore, droplet formation can occur either directly at the jet exit or further downstream, at the end of the liquid jet. These two types of instabilities are referred to as dripping and jetting, respectively.[8] Rayleigh[9] was the first to use linear stability analysis to investigate liquid jet instability. He derived the dispersion relation between the growth rate and the wavenumber for an inviscid liquid jet. Weber[10] performed a similar analysis to Rayleigh, but

for an incompressible viscous liquid jet with dynamic viscosity. He showed that the breakup length of the liquid jet depends linearly on its velocity. He found that the jet viscosity increases the wavelength of unstable modes, consequently leading to an increase in breakup times. Middleman[11] examined the instability of a viscoelastic liquid jet and compared the growth rate of surface disturbances along viscoelastic and viscous liquid jets. He found that viscous jets are more stable than viscoelastic jets. Goldin *et al.*[12] performed a similar analysis and found that the growth rate of disturbances along viscoelastic jets is smaller than the equivalent for inviscid jets but is higher than that of viscous jets for the same liquid jet of zero shear viscosity. Papageorgiou[13] developed an asymptotic approach to investigate the breakup of a viscous thread under different initial conditions. The effect of gravity on the instability of Newtonian liquid jets has been investigated by Cheong and Howes,[14] who used a finite difference solution to simulate drop formation. They also performed some experiments to compare with their numerical results. They noted that disturbance frequencies will decrease when the relative importance of gravity increases. Sauter and Buggisch[15] used linear instability analysis for viscous liquid jets falling vertically under gravity. They found a new global instability mode for viscous jets. Alsharif[16] investigated the linear temporal instability analysis of a viscoelastic

liquid jet falling under the influence of gravity. He used an asymptotic approach to obtain a simplified form of the governing equations and used the upper-convected Maxwell (UCM) model (which is a special case of the Oldroyd-B model) to describe the dynamics of the jet. He found that the temporal growth rate of a viscoelastic jet is increased by the influence of gravity. In addition, Ye, Yang, and Fu[17] investigated the temporal instability of viscoelastic compound liquid jets. They observed that the temporal growth rate is higher than the equivalent growth rate of a Newtonian compound jet.

The first work to demonstrate the existence of absolute instability in liquid jets was that of Leib and Goldstein.[18] They demonstrated that capillary instabilities for a slow moving inviscid jet eventually lead to absolute instability at small Weber numbers due to surface tension. They determined a critical value for the ratio of inertia to surface tension forces [denoted by the Weber number (We)] which marks the transition between convective and absolute instabilities. They showed that for $We > 3.15$, the jet is convectively unstable; while for $We < 3.15$, it is absolutely unstable. Leib and Goldstein[19] included the effect of viscosity and found that this leads to a decrease in the critical value of the Weber number when the Weber number is a function of the Reynolds number (Re). They plotted the relationship between the Reynolds number and the Weber number in the Re–We plane and found a critical curve that separates the region between convective and absolute instabilities. Briggs[20] developed a criterion for absolute instability analysis by looking at Fourier transformations of the dispersion relation and finding its solution in the complex wavenumber and frequency plane. This method was used by Lin and Lian[21] to find the boundary in a parameter map between convective and absolute instabilities for a viscous liquid jet when taking into account the influence of the surrounding gas. O'Donnell, Chen, and Lin[22] determined the critical value of the Weber number experimentally, indicating the beginning of absolute instability by taking into account the influence of gas viscosity. They demonstrated the existence of regions of absolute instability for viscous liquid jets under large Reynolds numbers when immersed in a viscous gas. Lin and Ibrahim[23] analyzed the convective and absolute instability of a viscous liquid jet surrounded by a viscous gas in a vertical pipe. They found that the critical curve in parameter space does not rely strongly on the ratio between gravity and inertia, jet diameter, and viscosity ratios. The influence of gravity on the growth rate of convective and absolute instabilities of an axisymmetric viscous jet has been studied by Amini and Ihme.[24] They performed a spatial instability analysis of the governing equations using a multiscale expansion technique to derive the dispersion relation, which they used for evaluating the growth rate of disturbances. They showed that the growth rate of instabilities is increased by gravity. Yang, Tong, and Fu[25] investigated the instability of axisymmetrical and nonaxisymmetrical disturbances for a column of a viscoelastic liquid jet moving in a swirling air stream. They showed that a three-dimensional viscoelastic liquid jet is more unstable than the Newtonian case when the air swirl is taken into account. They found that a decrease in the ratio of the time constant or an increase in the liquid elasticity leads to an increase in the maximum temporal growth rate.

In this paper, we examine the convective and absolute instability of an axisymmetrical viscoelastic liquid jet falling under gravity. This work extends the analysis of Alsharif[16] by including spatial and absolute instability analysis. We use a mapping technique,

often referred to as the "Cusp Map Method" developed by Kupfer, Bers, and Ram[1] to find the cusp point, which corresponds to the pinch point for absolute instability.

II. FORMULATION OF PROBLEM

Consider an axisymmetric column of an incompressible viscoelastic liquid jet, which has radius a, density ρ, and surface tension σ, emerging from a nozzle and falling under gravity. In order to consider the axisymmetric problem, we assume that the cross section of the jet remains circular ($\frac{\partial}{\partial \theta} = 0$) and swirl will not be considered ($v_\theta = 0$). Thus, the velocity vector takes the form $\mathbf{v} = (v_r, 0, v_z)$. The governing equations and the boundary conditions can be written in cylindrical coordinates, where the z-axis can be chosen as a parallel axis to the flow direction and the r-axis is perpendicular to the axis of symmetry for the liquid jet column, as shown in Fig. 1. We assume for simplicity that the surrounding medium is quiescent and that its effects are negligible in the present problem.

A. The governing equations

According to Bird, Armstrong, and Hassager,[26] the relationship between the stress and strain in a viscoelastic liquid can be described by the Oldroyd-B constitutive equation

$$\mathbf{T} + \lambda \mathbf{T}^{\diamond} = \mu_0 \left(\dot{\mathbf{D}} + \lambda_r \dot{\mathbf{D}}^{\diamond} \right), \qquad (1)$$

where $\mathbf{T}$ is the extra stress tensor (this brings the elastic effect to the stresses), λ is the relaxation time, λ_r is the retardation time, μ_0 is the zero-shear viscosity (the total viscosity) composed of polymer and solvent components ($\mu_0 = \mu_p + \mu_s$), $\dot{\mathbf{D}}$ is the symmetric part of the strain rate tensor defined as $\dot{\mathbf{D}} = \nabla \mathbf{v} + (\nabla \mathbf{v})^T$, and the $\mathbf{T}^{\diamond}$ and $\dot{\mathbf{D}}^{\diamond}$ denote the upper convected time derivative of $\mathbf{T}$ and $\dot{\mathbf{D}}$, respectively, defined by

$$\mathbf{T}^{\diamond} = \frac{\partial \mathbf{T}}{\partial t} + (\mathbf{v} \cdot \nabla) \mathbf{T} - \mathbf{T} \cdot \nabla \mathbf{v} - (\nabla \mathbf{v})^T \cdot \mathbf{T},$$

where t is the time. Two special cases exist: the first case is when $\lambda = 0$, $\lambda_r = 0$, and $\mu_p = 0$, the Oldroyd-B model reduces to the linear constitutive equation for Newtonian fluids; the second case is when $\lambda \neq 0$, $\lambda_r = 0$, and $\mu_s = 0$, this model reduces to the upper-convected Maxwell (UCM) model for pure polymers[27] (this model has several
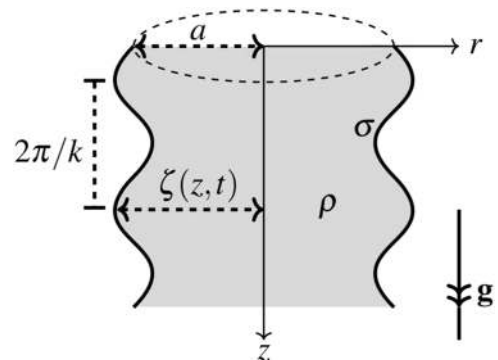

FIG. 1. A sketch of the viscoelastic liquid jet column of radius a in cylindrical coordinates with axisymmetrical surface disturbance.

properties of polymer solutions that can be captured to a good first approximation). Therefore, from the second case, the constitutive equation, (1), can be written as

$$\mathbf{T} = \mu_p \dot{\mathbf{D}} - \lambda \mathbf{T}^\diamond, \tag{2}$$

where μ_p is the polymer viscosity. Therefore, the governing equations are the continuity equation for an incompressible fluid, which is

$$\nabla \cdot \mathbf{v} = 0, \tag{3}$$

and the momentum equation, which is

$$\rho \left(\frac{\partial}{\partial t} + \mathbf{v} \cdot \nabla \right) \mathbf{v} = -\nabla p + \nabla \cdot \boldsymbol{\tau} + \rho \mathbf{g}, \tag{4}$$

where

$$\boldsymbol{\tau} = \mu_s \dot{\mathbf{D}} + \mathbf{T} = (\mu_s + \mu_p) \dot{\mathbf{D}} - \lambda \mathbf{T}^\diamond, \tag{5}$$

p is the pressure, $\mathbf{g} = (0, 0, g)$, and μ_s is the solvent viscosity. The position of the jet interface can be expressed as $r - \zeta(z, t) = 0$. Furthermore, this position has to be determined as a part of the solution to the flow equations, which is different from other flow situations that have known prior boundaries.

B. The boundary conditions

The boundary conditions at the free surface can be evaluated by expressing the pressure difference across the jet interface with the normal stress, which is related to the mean curvature, as follows:

$$\mathbf{n} \cdot \boldsymbol{\Pi} \cdot \mathbf{n} = \sigma \kappa, \tag{6}$$

where $\mathbf{n}$ is the outward unit normal vector to the jet interface, $\boldsymbol{\Pi}$ is the total stress tensor, which is given by $\boldsymbol{\Pi} = -p\mathbf{I} + \boldsymbol{\tau}$, and κ is the mean curvature of the liquid jet defined by

$$\kappa = \frac{1}{E\zeta} - \frac{1}{E^3} \frac{\partial^2 \zeta}{\partial z^2}, \text{ where } E = \left(1 + \left(\frac{\partial \zeta}{\partial z} \right)^2 \right)^{\frac{1}{2}}.$$

The tangential stresses are equated to zero along the jet interface

$$\mathbf{t} \cdot \boldsymbol{\Pi} \cdot \mathbf{n} = 0, \tag{7}$$

where $\mathbf{t}$ is the tangential unit vector. Finally, the kinematic boundary condition, which requires a liquid particle on the interface to remain on the interface, can be expressed as

$$\frac{D}{Dt} \left(r - \zeta(z, t) \right) = 0, \tag{8}$$

where $\frac{D}{Dt} = \frac{\partial}{\partial t} + \mathbf{v} \cdot \nabla$ is the material derivative.

III. DIMENSIONLESS ANALYSIS

Following Anno,[28] the governing equations and the boundary conditions can be written in nondimensional form by using the following nondimensional scales:

$$z^* = \frac{z}{L}, \quad r^* = \frac{r}{a}, \quad t^* = \frac{U}{L}t, \quad p^* = \frac{p}{U^2 \rho}, \quad \varepsilon = \frac{a}{L},$$

$$v_r^* = \frac{v_r}{U}, \quad v_z^* = \frac{v_z}{U}, \quad \zeta^* = \frac{\zeta}{a}, \quad T^* = \frac{L}{U\mu_0}T, \tag{9}$$

where U is the jet exit velocity, L is the scale of the axial length, $0 < \varepsilon \ll 1$, μ_0 is the total viscosity, and $\mathbf{T}$ is the additional stress tensor. After dropping the superscript (*), the dimensionless parameters that enable us to analyze the flow dynamics of a viscoelastic liquid jet falling under gravity are

$$Re = \frac{U\rho a}{\mu_0}, \quad \alpha = \frac{\mu_s}{\mu_0}, \quad We = \frac{\rho U^2 a}{\sigma}, \quad F = \frac{U}{\sqrt{ag}}, \quad De = \frac{\lambda U}{L}, \tag{10}$$

where Re is the Reynolds number (which is a measure showing the relative importance between viscous forces and inertia), α is the ratio of solvent viscosity to the total viscosity, We is the Weber number (which is a measure of the relative importance of inertia to surface tension), F is the Froude number, and De is the Deborah number (which is a measure of the amount of time it takes to reach a specific reference strain). Using typical values obtained in industrial applications of viscoelastic fluids (see Verhoef, Van den Brule, and Hulsen[29] and Bird et al.[30]), where $\lambda \sim 10^{-3}$–10 and $\mu_0 \sim 10^{-2}$–10, we can see that for a liquid jet of diameter $a = 10^{-3}$ m and having initial speed $U \sim 0.3$–10 ms^{-1}, we have $De \sim 10^{-2}$–10^3 and $Re \sim 10^{-2}$–10^2. In the subsequent analysis, we use parameter values which fall within these regimes. The dimensionless forms of the governing equations and the boundary conditions can be found in Appendix A.

IV. ASYMPTOTIC ANALYSIS

Following Eggers,[31] we assume that the jet is slender (i.e., we define a small aspect ratio $\varepsilon = a/L \ll 1$). Therefore, we examine our dimensionless expressions (in Appendix A) in more detail by expanding v_r, v_z, and p in a Taylor series in εr; and ζ, T_{rr}, and T_{zz} in an asymptotic series in ε. Furthermore, we assume that the centerline of the liquid jet column is not affected by small perturbations. In the long wave limit when $\zeta(z)$ varies slowly with respect to z, the axial velocity, pressure, and the stress components T_{zz} and T_{rr} are almost uniform with respect to r, while the off-diagonal stress component T_{rz} is nearly zero. Hence, the proper ansatz for slender jets is a Taylor expansion in r. Therefore, we have

$$\{v_r, v_z, p\} = \{v_{r0}(z, t), v_{z0}(z, t), p_0(z, t)\}$$
$$+ \varepsilon r \{v_{r1}(z, t), v_{z1}(z, t), p_1(z, t)\} + O(\varepsilon^2 r^2), \tag{11}$$

$$\{\zeta, T_{rr}, T_{zz}\} = \{\zeta_0(z, t), T_{rr}^0(z, t), T_{zz}^0(z, t)\}$$
$$+ \varepsilon \{\zeta_1(z, t), T_{rr}^1(z, t), T_{zz}^1(z, t)\} + O(\varepsilon^2). \tag{12}$$

Considering our governing equations and in order to retain viscoelastic terms and gravitational terms, we need to rescale the Reynolds number $Re/\varepsilon = \tilde{Re} = O(1)$ and the Froude number $\varepsilon F^2 = \tilde{F}^2 = O(1)$ (for more details, see Uddin[32]). Therefore, after substituting the expressions, (11) and (12), into our dimensionless forms (in Appendix A) and dropping the tildes for convenience, from the axial momentum equation, we have

$$O(\varepsilon): \frac{\partial v_{z0}}{\partial t} + v_{z0} \frac{\partial v_{z0}}{\partial z} = \frac{-1}{We} \frac{\partial}{\partial z} \left(\frac{1}{\zeta_0} \right) + \frac{3\alpha}{\zeta_0^2 Re} \frac{\partial}{\partial z} \left(\zeta_0^2 \frac{\partial v_{z0}}{\partial z} \right)$$
$$+ \frac{1}{\zeta_0^2 Re} \frac{\partial}{\partial z} \left(\zeta_0^2 (T_{zz}^0 - T_{rr}^0) \right) + \frac{1}{F^2}. \tag{13}$$

For more details of the derivation of the equation, (13), see Appendix B. The components of the extra stress tensor, (A4) and (A5), to leading order become, respectively,

$$\frac{\partial T_{zz}^0}{\partial t} + v_{z0}\frac{\partial T_{zz}^0}{\partial z} - 2T_{zz}^0\frac{\partial v_{z0}}{\partial z} = \frac{1}{De}\left(2(1-\alpha)\frac{\partial v_{z0}}{\partial z} - T_{zz}^0\right), \quad (14)$$

$$\frac{\partial T_{rr}^0}{\partial t} + v_{z0}\frac{\partial T_{rr}^0}{\partial z} + T_{rr}^0\frac{\partial v_{z0}}{\partial z} = \frac{-1}{De}\left((1-\alpha)\frac{\partial v_{z0}}{\partial z} + T_{rr}^0\right). \quad (15)$$

If $F \to \infty$, the last set of Eqs. (13)–(15) are the same as those obtained by Clasen et al.[33] The kinematic condition to leading order becomes

$$\frac{\partial \zeta_0}{\partial t} + \frac{\zeta_0}{2}\frac{\partial v_{z0}}{\partial z} + v_{z0}\frac{\partial \zeta_0}{\partial z} = 0. \quad (16)$$

V. THE STEADY STATE SOLUTIONS

In order to obtain the steady state solutions of (13)–(16), we set all time derivatives to zero and consider this nonlinear system of equations involving the four variables v_{z0}, ζ_0, T_{zz}^0, and T_{rr}^0 as functions of z. From (16), we find that $\zeta_0^2 v_{z0}$ is constant, and from the boundary condition at the nozzle, where $v_{z0}(0) = 1$ and $\zeta_0(0) = 1$, we find that $\zeta_0^2 v_{z0} = 1$. Therefore, Eqs. (13)–(15) become, respectively,

$$v_{z0}\frac{\partial v_{z0}}{\partial z} = \frac{-1}{2\sqrt{v_{z0}}We}\frac{\partial v_{z0}}{\partial z} + \frac{3\alpha}{Re}\left(\frac{\partial^2 v_{z0}}{\partial z^2} - \frac{1}{v_{z0}}\left(\frac{\partial v_{z0}}{\partial z}\right)^2\right)$$
$$+ \frac{1}{Re}\left(\frac{\partial}{\partial z}(T_{zz}^0 - T_{rr}^0) - \frac{1}{v_{z0}}\frac{\partial v_{z0}}{\partial z}(T_{zz}^0 - T_{rr}^0)\right) + \frac{1}{F^2}, \quad (17)$$

$$De\left(v_{z0}\frac{\partial T_{zz}^0}{\partial z} - 2T_{zz}^0\frac{\partial v_{z0}}{\partial z}\right) = 2(1-\alpha)\frac{\partial v_{z0}}{\partial z} - T_{zz}^0, \quad (18)$$

$$De\left(v_{z0}\frac{\partial T_{rr}^0}{\partial z} + T_{rr}^0\frac{\partial v_{z0}}{\partial z}\right) = -(1-\alpha)\frac{\partial v_{z0}}{\partial z} - T_{rr}^0. \quad (19)$$

We have three nonlinear ordinary differential Eqs. (17)–(19), in three unknowns v_{z0}, T_{rr}^0, and T_{zz}^0. To solve these equations as an initial boundary value problem, we need the boundary conditions at $z = 0$. Besides the boundary condition for v_{z0}, the other conditions are not immediately obvious. To determine a consistent set of boundary conditions at the nozzle, $z = 0$, we expand our variables for $z \to 0$ as follows:

$$\{v_{z0}, T_{rr}^0, T_{zz}^0\} = \{1, \gamma_0, s_0\} + \{c_1, \gamma_1, s_1\}z + \{c_2, \gamma_2, s_2\}z^2 + \dots.$$

We then substitute these expressions into the last set of equations and equate coefficients of $O(1)$ to zero to obtain a system of nonlinear equations. These can be solved to establish a consistent set of boundary conditions as $z \to 0$. We assume, in line with other studies which consider a similar problem Deshawar and Chokshi[34] and Riahi et al.,[35] that the boundary condition for the extra stress terms can be approximated by their Newtonian equivalent [that is, setting $De = 0$ in (18) and (19)]. This leads to $s_0 = 2(1-\alpha)c_1$ and $\gamma_0 = (\alpha - 1)c_1$. Using this assumption and then substituting our small z expansion into (17), we obtain a quadratic equation for c_1 (similar to that found in Nonnenmacher and Piesche[36]) which depends on the coefficient of the axial velocity term at $O(z^2)$—that is, c_2.
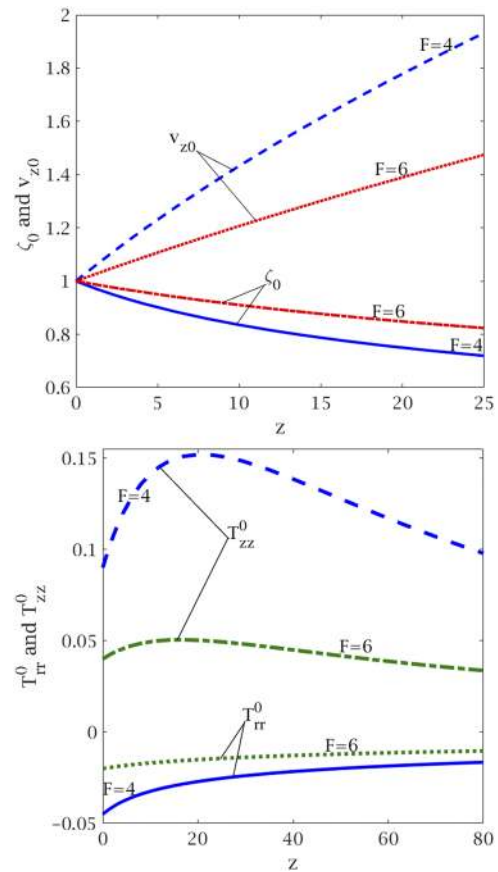

FIG. 2. Graph showing values of ζ_0, v_{z0}, T_{rr}^0, and T_{zz}^0 against z for different values of F, where $De = 10$, $Re = 800$, $We = 2$, and $\alpha = 0.03$.

This is similar to the situation in Riahi et al.[35] where a viscoelastic liquid jet emerging from a rotating spinneret was considered. Similar to that work, we too find that the value of c_2 has little impact on the solution for c_1 and we likewise set $c_2 = 0$. In doing so, we incorporate the fact that as the jet is accelerating due to gravity, we expect $\partial v_{z0}/\partial z > 0$. Given that as the liquid emerges from the nozzle, it loses traction and undergoes local flow changes which can be important for viscoelastic jets (die swell), which we do not consider here, the above choice of boundary conditions (which is consistent with our set of equations) provides a viable framework with which to examine this problem. We solve the nonlinear ordinary differential Eqs. (17)–(19), by using MATLAB (ode45), which is based on the Runge-Kutta method. The effect of gravity (through the Froude number) on steady state solutions is shown in Fig. 2. It can be seen that a reduction in the Froude number leads to the jet thinning more quickly and also the axial velocity increasing more quickly along the jet.

VI. LINEAR INSTABILITY ANALYSIS

The jet develops over the length scale $z = O(1)$. However, waves along the jet are much smaller and typically have

wavelengths of $O(a)$—which are comparable to ε in the case of $z = O(1)$. This multiscale approach has been used by Uddin.[32] Using $exp(ik\bar{z} + \omega\bar{t})$ as a traveling wave mode model, where $z = \varepsilon\bar{z}$, $t = \varepsilon\bar{t}$, $k = k(z) = O(1)$ and $\omega = \omega(z) = O(1)$. We apply a small perturbation around the steady state solutions. Therefore, we have the substitutions

$$
\begin{aligned}
\{v_r, v_z, \zeta, T_{rr}, T_{zz}, p\} = & \{0, v_{z0}(z), \zeta_0(z), T_{rr}^0(z), T_{zz}^0(z), p_0(z)\} \\
& + \xi\{\bar{v}_r(r), \bar{v}_z(r), \bar{p}(r), \bar{\zeta}, \bar{T}_{rr}(r), \bar{T}_{zz}(r)\} \\
& \times e^{(ik(z)\bar{z} + \omega(z)\bar{t})},
\end{aligned}
\tag{20}
$$

where $0 < \xi \ll 1$ is a small dimensionless number. By substituting these expressions into our dimensionless forms (in Appendix A), replacing $\alpha/\varepsilon = \tilde{\alpha} = O(1)$ (this corresponds to examining large values of μ_p), keeping terms of $O(\xi)$ only, and after dropping the tildes for convenience, we obtain a set of ordinary differential equations (see Appendix C). Therefore, it can be shown after solving these differential equations and applying the tangential and kinematic boundary conditions that the final forms of the pressure and velocity profiles ($\bar{p}$, $\bar{v}_r$ and $\bar{v}_z$) can be written, respectively, as

$$
\begin{aligned}
\bar{p} = & -\left\{\frac{2hk^2(T_{rr}^0 + \frac{1}{De})}{Re\Lambda}\left(\frac{\alpha(1+c)\Lambda + c(T_{rr}^0 - T_{zz}^0)}{\alpha(ch^2 - k^2)}\right)\frac{I_0(hr)}{I_1(h\zeta_0)}\right. \\
& + \left(\frac{\sqrt{c}k(\alpha(h^2 + k^2)\Lambda + k^2(T_{rr}^0 - T_{zz}^0))}{\alpha(ch^2 - k^2)}\right) \\
& \times \left.\left(\frac{\Lambda}{k^2} + \frac{2(T_{zz}^0 + \frac{1}{De})}{Re\Lambda}\right)\frac{I_0(kr/\sqrt{c})}{I_1(k\zeta_0/\sqrt{c})}\right\}\bar{\zeta},
\end{aligned}
\tag{21}
$$

$$
\begin{aligned}
\bar{v}_r = & \left\{\left(\frac{c\alpha(h^2 + k^2)\Lambda + ck^2(T_{rr}^0 - T_{zz}^0)}{\alpha(ch^2 - k^2)}\right)\frac{I_1(kr/\sqrt{c})}{I_1(k\zeta_0/\sqrt{c})}\right. \\
& - \left.\left(\frac{\alpha(1+c)k^2\Lambda + ck^2(T_{rr}^0 - T_{zz}^0)}{\alpha(ch^2 - k^2)}\right)\frac{I_1(hr)}{I_1(h\zeta_0)}\right\}\bar{\zeta},
\end{aligned}
\tag{22}
$$

$$
\begin{aligned}
\bar{v}_z = & i\left\{\left(\frac{\sqrt{c}\alpha(h^2 + k^2)\Lambda + \sqrt{c}k^2(T_{rr}^0 - T_{zz}^0)}{\alpha(ch^2 - k^2)}\right)\frac{I_0(kr/\sqrt{c})}{I_1(k\zeta_0/\sqrt{c})}\right. \\
& - \left.\left(\frac{\alpha(1+c)kh\Lambda + ckh(T_{rr}^0 - T_{zz}^0)}{\alpha(ch^2 - k^2)}\right)\frac{I_0(hr)}{I_1(h\zeta_0)}\right\}\bar{\zeta},
\end{aligned}
\tag{23}
$$

where

$$
c = \frac{\alpha\Lambda(D_0 - h^2)}{2k^2(T_{rr}^0 + T_{zz}^0 + \frac{2}{De}) + \alpha\Lambda(D_0 - h^2) + \frac{2}{r^2}(T_{rr}^0 + \frac{1}{De})},
$$

$$
h^2 = k^2 + \frac{Re\Lambda}{\alpha} + \frac{2k^2}{\alpha\Lambda}\left(T_{zz}^0 + T_{rr}^0 + \frac{2}{De}\right),
$$

$\Lambda = (\omega + ikv_{z0})$, and I_1 and K_1 are the first and the second kind of the modified Bessel function of the first order, respectively. By substituting these solutions, (21)–(23), into the normal stress boundary condition, (C6), we obtain the following dispersion relation:

$$
\begin{aligned}
& \Lambda^2 + \frac{2k^2}{Re}\left(T_{zz}^0 + \frac{1}{De}\right) + \frac{2k^2}{Re}\left(\alpha\Lambda + \left(T_{rr}^0 + \frac{1}{De}\right)\right)\frac{I_1'(k\zeta_0/\sqrt{c})}{I_0(k\zeta_0/\sqrt{c})} \\
& + \frac{2hk^3}{Re}\left(\frac{\alpha(1+c)\Lambda + c(T_{rr}^0 - T_{zz}^0)}{\sqrt{c}(\alpha(h^2 + k^2)\Lambda + k^2(T_{rr}^0 - T_{zz}^0))}\right)\frac{I_1(k\zeta_0/\sqrt{c})}{I_0(k\zeta_0/\sqrt{c})} \\
& \times \left(\left(T_{rr}^0 + \frac{1}{De}\right)\left(\frac{I_0(h\zeta_0)}{I_1(h\zeta_0)} - \frac{I_1'(h\zeta_0)}{I_1(h\zeta_0)}\right) - \Lambda\alpha\frac{I_1'(h\zeta_0)}{I_1(h\zeta_0)}\right) \\
& = \left(\frac{\Lambda k\alpha(ch^2 - k^2)(1 - k^2\zeta_0^2)}{\sqrt{c}(\alpha\Lambda(h^2 + k^2) + k^2(T_{rr}^0 - T_{zz}^0))We\zeta_0^2}\right)\frac{I_1(k\zeta_0/\sqrt{c})}{I_0(k\zeta_0/\sqrt{c})}.
\end{aligned}
\tag{24}
$$

VII. CONVECTIVE INSTABILITY ANALYSIS

There are two different types of convective instabilities: temporal instability, where the wavenumber is real and the frequency is complex, and spatial instability, where the frequency is purely imaginary and the wavenumber is complex.

A. Temporal instability analysis

Here, we are interested in describing the temporal instability of viscoelastic liquid jets and so we consider in our dispersion relation, (24), a complex frequency ($\omega = \omega_r + i\omega_i$, where ω_r symbolizes the disturbance growth rate and ω_i symbolizes 2π times frequency of the disturbance) and a real wavenumber k. We use the Newton-Raphson method to solve the dispersion relation. The most unstable wavenumber is defined as the wavenumber that leads to the largest value of $Re(\omega)$. In general, the steady state values (see Sec. V) will change with z, and hence, the associated most unstable wavenumber and the corresponding growth rate will also vary in the downstream direction of the jet.[32]

We plot the relationship between the growth rate (ω_r) and the wavenumber of the viscoelastic liquid jet, for different Weber numbers, in Fig. 3. It can be seen that when we decrease the Weber number (which corresponds to a greater influence of surface
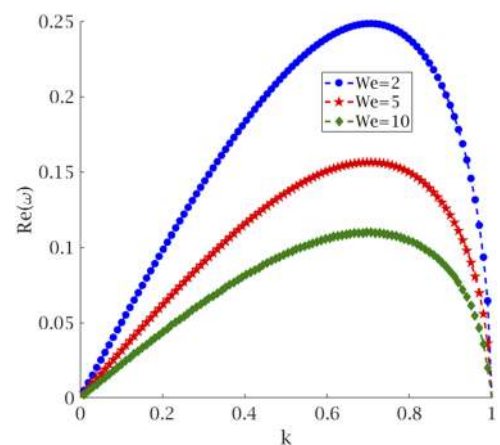
FIG. 3. Graph showing the growth rate ω_r against the wavenumber k for various values of the Weber number, where $F = 4$, $Re = 800$, $\alpha = 3$, and $De = 10$ at $z = 0$.
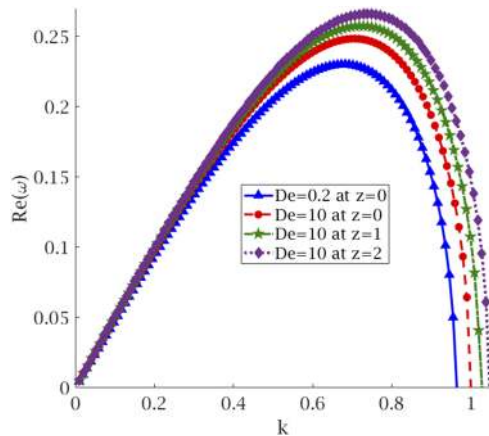
FIG. 4. Graph showing the relationship between ω_r and k for various values of z and the Deborah number, where $F = 4$, $Re = 800$, $\alpha = 3$, and $We = 2$.
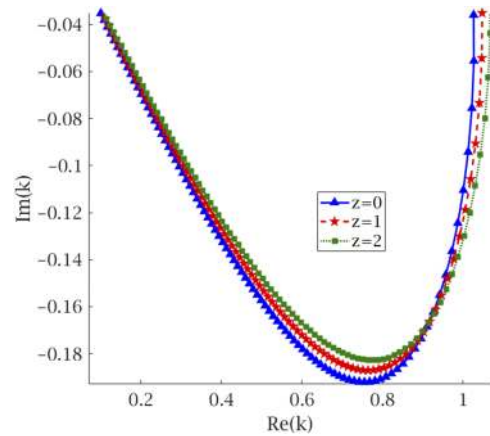

FIG. 6. Graph showing the spatial growth rate against the wavenumber for various values of the axial length of the viscoelastic jet, where $We = 4$, $De = 10$, $\alpha = 3$, $F = 4$, and $Re = 800$.

tension over inertia), the growth rate increases leading to shorter jets. In Fig. 4, we plot the temporal growth rate for various values of the Deborah number and the axial locations of the jet (z). We can see that the maximum value of the temporal growth rate and the most unstable wavenumber are increased along the jet (for different values of z) or by increasing the Deborah number. In addition, we note that the range of instability is increased along the jet by increasing the Deborah number. The most unstable wavenumber can be seen as an inverse measure (through the wavelength) of the predicted droplet sizes. In this respect, Fig. 4 would suggest that increasing the Deborah number will lead to reduced droplet sizes and shorter jets. This result is in line with observations by Brenn, Liu, and Durst[37] and Ruo et al.[38] where the disturbance growth rate of viscoelastic liquid jets approaches the corresponding growth rates of Newtonian liquid jets when $De \to 0$ and $\mathbf{T} \to 0$.
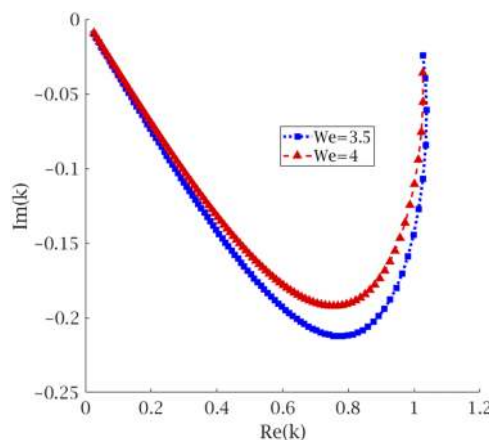

FIG. 5. Graph showing the relationship between $Im(k)$ and $Re(k)$ for different values of the Weber number, where $De = 10$, $F = 4$, $\alpha = 3$, and $Re = 800$ at $z = 0$.

B. Spatial instability analysis

A more physically realistic scenario for stability has been proposed by Keller, Rubinow, and Tu[39] which is known as spatial stability. They observed that disturbances on the jet surface can grow in space rather than with time, where k is assumed to be complex, while ω is purely imaginary. According to Busker, Lamers, and Nieuwenhuizen,[40] the spatial instability can better describe the physical process of the liquid jet breakup. Spatial instability can also be used to simulate satellite formation before or after the main droplet formation based on the disturbance amplitude. A comparison between the theoretical prediction and the experimental results observed by Si et al.[41] indicates that the results of spatial instability are better aligned with experiments than the analysis of the temporal instability, especially for moderate to high Weber numbers.[42]

In this section, following Keller, Rubinow, and Tu,[39] we consider a wave mode of the form $exp(ik\tilde{z} - i\omega\tilde{t})$, but in this case, k is assumed to be complex and ω is the real frequency of the wave mode. For unstable disturbances, we require $Im(k) < 0$ where the most negative number gives the maximum value of the spatial growth rate. The dispersion relation, (24), is solved numerically using the Newton-Raphson method for k with given values of ω. We show the relationship between $Im(k)$ and $Re(k)$ for different values of the Weber number in Fig. 5. It is clear, from Fig. 5, that the maximum value of the spatial growth rate will be increasing when the Weber number is increased. While, we note from Fig. 6, that the range of instability and the maximum value of the spatial growth rate are increased along the viscoelastic jet.

VIII. ABSOLUTE INSTABILITY ANALYSIS

In liquid jets, different types of instabilities can be categorized depending on the movement and shape of wave packets growing along the jet. The flow is said to be absolutely unstable when whole wave packets drift upstream or downstream, and where disturbances can grow with time at all fixed spatial positions. Otherwise, we say that the flow is convectively unstable.[43] Convective instability grows and propagates away from its point of origin. This causes a rupture

in the jet elsewhere away from the point of origin as well as leaving the jet unaffected at the point of origin. In contrast, absolute instability propagates far from its point of origin, but at the same time destabilizes the jet everywhere, including at the origin of the disturbance. Based on the work of Briggs,[20] the criterion for absolute instability of a wave mode of the form $e^{(\omega t + ikz)}$, where k and ω are taken as complex numbers, is if the solution of the dispersion relation is a first-order saddle point in the complex k-plane, which corresponds to a pinch point (a cusp point) in the complex ω-plane. A "cusp point" appears when an intersection occurs between $k(\omega)$ curves in the complex-frequency plane. Absolute instability requires that the dispersion relation solution has $Re(\omega) > 0$.[44] To confirm that the absolute instability will occur when the group velocity (which is defined by $\partial\omega/\partial k$) is zero at the saddle point k_0 (which is a necessary condition, but it is not a sufficient condition). This is because the group velocity is zero not only at saddle points but also when two k-branches meet independently of whether the branches originated from the same half-k-plane or not. To overcome this, Kupfer, Bers, and Ram[1] developed a mapping procedure in which pinch points can be found by using mappings of chosen contour lines from the complex k-plane into the complex ω-plane. When the contour lines are deformed, a branch point arises up in the ω-plane which is called a cusp point. At the same time, a pinch point appears in the k-plane. Further deformations of contour lines after forming the pinch point lead to a violation of causality, and these deformations are stopped. To determine if the cusp point has been formed by the continuous analysis of k-branches creating from two different halves of k-plane or not, the following procedure can be followed. According to Kupfer, Bers, and Ram,[1] one can check that the cusp point is a pinch point by drawing a straight ray parallel to the ω_r-axis from the cusp point to the image of the first contour line (for $k_i = 0$) and then counting the number of points that this ray intersects with the image of the first contour line. If the number of intersections between this ray and the image of the first contour line is odd, then this cusp point has been formed by two k-branches creating from two different halves of the k-plane and the cusp point is named as a pinch point.[1]

A. Finding the cusp point

Kupfer, Bers, and Ram[1] have shown that mappings from the complex-frequency plane to the wavenumber plane, through the dispersion relation $D(\omega, k) = 0$, can identify absolute instability. However, for many physical systems, the dispersion relation is a polynomial in ω while transcendental in k. It is easier to solve for ω given a k than it is to solve for k given an ω. Kupfer, Bers, and Ram have also shown that mappings of successive deformations of the Fourier integral path along the real k-axis in the ω-plane, points satisfying $\frac{\partial D}{\partial k} = 0$ are easily discovered by the characteristic property of their local maps. They found that there is a topological relationship between these points and that the image of the real k-axis determines the characteristics of stability.

Since it is easier to map from the complex wavenumber plane to the frequency plane this allows us to determine stability characteristics without solving transcendental equations. The image of this area in the k-plane will be bounded by the first contour produced by mapping the real line from the complex wavenumber plane on one side. There are many contour lines along the scope of the unstable

wavenumbers. When the contour lines are mapped into the ω-plane, every contour line finishes and leaves its image in this specific area. The parallel lines of constant $Im(k) < 0$ mapped onto the complex frequency plane may produce a cusp point. If a cusp point can be identified, it will correspond to a value ω_0 in the complex frequency plane. This point will have been produced by an associated value of $k = k_0$ in the complex wavenumber plane. By definition, $D(\omega_0, k_0) = 0$ and $\partial D(\omega_0, k_0)/\partial k = 0$. If k_0 and ω_0 are such that $\partial^2 D(\omega_0, k_0)/\partial k^2 \neq 0$, then we have identified a pinch point. Therefore, $\omega = \omega_0$ is the position of the cusp point in the complex ω-plane and $k(\omega_0)$ is the position of the saddle point in the k-plane corresponding to the cusp point ω_0. It is easy to infer that the relationship, $\omega - \omega_0 \sim (k - k_0)^2$, is a fundamental characteristic to form the branch point (the cusp point) in the complex ω-plane, on condition that the pinch point in the complex k-plane is a first-order saddle point, which is defined as the corresponding point to the cusp point in the ω-plane. Finding the cusp point requires searching the k plane by using k_r-contour lines for different values of $k_i < 0$ and plotting the images of the contour lines in the complex ω-plane. These images of the contour lines form a cusp when they are close to the singularity. On one of these contour lines, the exact cusp point (ω_0) will appear. After identifying the cusp point, we can determine stability by identifying the sign of ω_0. If $\omega_{0r} > 0$, the flow is absolutely unstable; either if this point is formed in the left half of the ω-plane, i.e., if $\omega_{0r} < 0$, the system is convectively unstable, provided that is in the situation where the system is already temporal unstable flow; otherwise, the system is stable.[45]

According to the Kupfer, Bers, and Ram method, the cusp line is a set of points in the ω-plane that can be found by considering the mappings of lines of $Im(k) = k_i^*$ (constant) in the complex k-plane onto the ω plane. This is done for successive values of k_i^* from zero to down to a constant negative value. By using this method when $k_i = 0$ and varying k_r (k_r-contour line), the image of the first contour line (for $k_i = 0$) of the dispersion relation corresponds to the temporal growth rate result as shown in Fig. 3 when $We = 2$. By reducing k_i^* to negative values gives the corresponding images of the dispersion relation, (24), in the ω-plane as shown in Fig. 7. For k_r-contour lines when $k_i = -0.244$, we notice the emergence of a cusp point at $\omega_0 = 0.0728 - 0.831i$ as shown in Fig. 7, which corresponds to the saddle point (the pinch point), k_0, in the complex k-plane. This cusp point is a pinch point because when we draw a straight ray parallel to the ω_r-axis from the cusp point to the image of the first k_r-contour line (for $k_i = 0$) in the complex ω-plane, we find one intersection point only (odd number).[46,47] For a reference state in this section, $De = 10$, $\alpha = 3$, $F = 4$, $Re = 800$, and $We = 2$ at $z = 0$, the flow is absolutely unstable because of $\omega_{0r} > 0$ as shown in Fig. 7.

B. Finding the saddle point

Following Bassi[7] and Balestra, Gloor, and Kleiser,[48] we use the saddle point method to find solutions of the dispersion relation, i.e., $D(\omega, k) = 0$, for the complex pair (ω_0, k_0), where $D(\omega_0, k_0) = \partial D(\omega_0, k_0)/\partial k = 0$ and $\partial^2 D(\omega_0, k_0)/\partial k^2 \neq 0$. In order to investigate the behavior of changing dimensionless parameters, we consider a reference state, where $We = 2$, $F = 4$, $Re = 800$, $\alpha = 3$ and $De = 10$ at $z = 0$. The dispersion relation, (24), is then solved for spatial curves to find the saddle point in the complex k-plane. In general, there are two distinguished branches of spatial solutions for $D(\omega, k) = 0$,
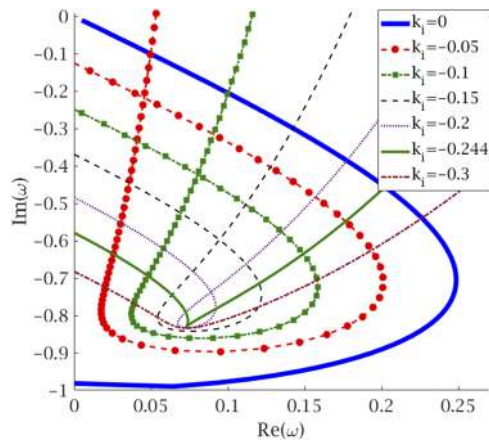
FIG. 7. Graph showing k_r-contour lines for different values of k_i in the complex ω plane. The thin green solid line is the cusp line for $k_i = -0.244$, which contains the cusp point at $\omega_0 = 0.0728 - 0.831i$, while the thick blue solid line is the first k_r-contour line for $k_i = 0$, where $De = 10$, $F = 4$, $\alpha = 3$, $Re = 800$, and $We = 2$ at $z = 0$.
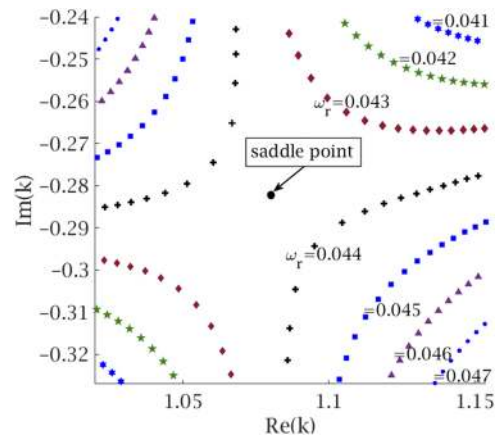

FIG. 8. Graph showing the saddle point, which is located at $k_0 = 1.0789 - 0.2844i$, between two spatial branches of the ω_i-contour line for $\omega_r = 0.043$ and $\omega_r = 0.044$, respectively, in the complex k-plane, where $\alpha = 3$, $F = 4$, $De = 10$, $We = 2$, and $Re = 800$ at $z = 0$.

where each branch contains a set of points located on both sides of the saddle point. These points are found by examining ω_i-contour lines and reducing ω_r from positive small values to zero, and then solving the dispersion relation for k numerically using the Newton-Raphson method. When the two branches of the ω_i-contour lines approach each other by reducing ω_r from positive small values to zero, a saddle point will occur at $k = k_0$.

Before finding the saddle point, it is important to note that the cusp point in the ω-plane corresponds to the pinch point (i.e., the first-order saddle point only) in the k-plane. This is because the group velocity (i.e., the velocity at which the wave packets are propagated) is zero not only at the saddle point but also when the two k-branches are met independently of whether the branches originated from the same half-k-plane or not. To ensure correct positions of the first-order saddle point, we need to use ω_i-contour lines for several positive small values of ω_r near the real part of the cusp point (ω_{0r}) in the complex k-plane. We then solve, using the Newton-Raphson method, the dispersion relation numerically for k. Using the above method, one finds that the first-order saddle point is located at $k_0 = 1.0789 - 0.2844i$, between two spatial curves (two ω_i-contour lines of $\omega_r = 0.043$ and $\omega_r = 0.044$) as shown in Fig. 8. We have checked that the cusp point (ω_0) and the saddle point (k_0) satisfy the saddle point conditions, which are $D(\omega_0, k_0) = \partial D(\omega_0, k_0)/\partial k = 0$ and $\partial^2 D(\omega_0, k_0)/\partial k^2 \neq 0$.[20,49]

C. Finding the convective/absolute instability boundary (CAIB)

To find the convective/absolute instability boundary (CAIB), we need to monitor the movement of the cusp point in the complex ω-plane as the Weber number increases when all other dimensionless parameters are fixed. We then use the Newton-Raphson method to find ω values at the cusp point. We repeat this process by gradually increasing the Weber number until we reach the value at which the ω_r changes sign from positive to negative (i.e., the critical value of $We = We_c$ at which the transition occurs from absolute instability

to convective instability, $\omega_{0r} = 0$), as shown in Fig. 9. This critical value of We (i.e., We_c) will mark the convective/absolute instability boundary (CAIB) between the convective and absolute regions.[50,51] We do the same thing for different values of the Reynolds number in the We–Re plane as shown in Fig. 10 and in the We–De plane to find the critical values of the Weber number corresponding to various values of the Deborah number, where We_c marks the CAIB in this plane as shown in Fig. 11. Moreover, CAIB is marked in the We–α plane by the critical values of the Weber number against various values of the viscosity ratio as shown in Fig. 12 using the same process above.
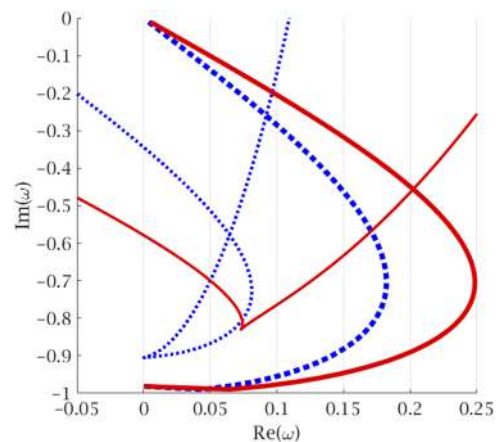

FIG. 9. Graph showing the movement of the cusp point in the complex ω-plane. The thin and thick red solid lines are the cusp line (for $k_i = -0.244$) and the first contour line (for $k_i = 0$), respectively, when $We = 2$; while the thin and thick blue dotted lines are the cusp line (for $k_i = -0.11$), where $\omega_{0r} = 0$ indicating the transition from absolute instability to convective instability, and the first contour (for $k_i = 0$), respectively, when $We = We_c = 3.7$, where $De = 10$, $F = 4$, $\alpha = 3$, and $Re = 800$ at $z = 0$.
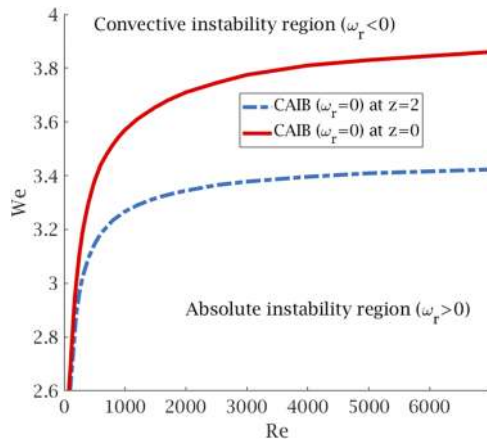
FIG. 10. Graph showing the convective/absolute instability boundary (CAIB), where We_c appears at $\omega_r = 0$, on the Re–We plane, where $De = 10$, $F = 4$, and $\alpha = 3$.
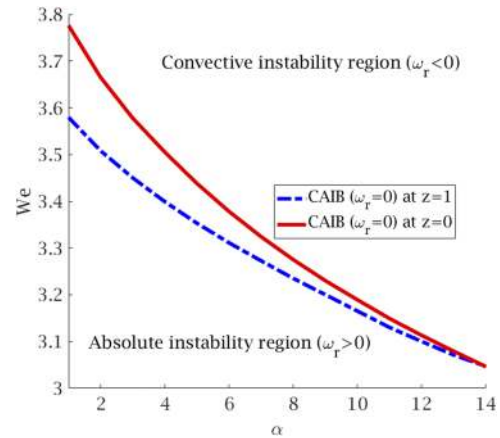

FIG. 12. Graph showing the convective/absolute instability boundary (CAIB), where We_c appears at $\omega_r = 0$, on the α–We plane, where $De = 10$, $F = 4$, and $Re = 800$.

In Fig. 10, we find that the CAIB increases as the viscosity decreases (the critical Weber number is increased by increasing the Reynolds number), but this boundary increases sharply in the range $(0 < Re < 500)$ and then increases gradually when $Re > 500$; this means that the transition from absolute instability to convective instability will be delayed when $We_c < 3.8$ at $z = 0$, while the transition is delayed when $We_c < 3.4$ at $z = 2$. In addition, we have seen, from Fig. 10, that the behavior in the CAIB is similar to that found by Lin and Lian[21,52] and López-Herrera, Gañán-Calvo, and Herrada.[53] From Fig. 11, we observe that the CAIB increases sharply in the range $(0 < De < 1)$ and then asymptotes, which indicates that the largest value of the critical Weber number is about $We = 3.7$ when $z = 0$, and does not go beyond $We = 3.8$, while the largest value of We_c is about $We = 3.4$ when $z = 1$. From Fig. 12, we note that the CAIB decreases with α (the critical Weber number decreases as the

viscosity ratio increases), which implies that the absolute instability will take place when the Weber number and the viscosity ratio are decreased together. In addition, from Fig. 12, we note that the largest value of We_c is decreased along the viscoelastic jet.

IX. CONCLUSION

We have examined the convective and absolute instability of a viscoelastic liquid jet falling under gravity. The upper-convected Maxwell (UCM) model is used along with an asymptotic approach to obtain steady state solutions. Perturbations to these solutions lead to a dispersion relation which is then solved numerically. We used a mapping technique developed by Kupfer, Bers, and Ram[1] to find the cusp point in the complex frequency plane and its corresponding saddle point (the pinch point) in the complex wavenumber plane for absolute instability. The convective/absolute instability boundary (CAIB) is identified for various parameter regimes. In particular, we have investigated the influence of the nonuniform nature (caused by the effects of gravity) of the steady state on instability. Our results demonstrate that the jet may become absolutely unstable at parameter values different from those found when using a constant radius steady state (which corresponds to $z = 0$ in our studies). Moreover, for fixed values of the Reynolds number, Deborah number, and α, we see that the jet will be absolutely unstable for lower values of the Weber number. In applications where absolute instability is sought (e.g., spray formation), there will be reduced scope for changing the Weber number.

The results within this work will have applications to industrial processes where viscoelastic liquid jets are used. These include recent advances in needle-free injections where a recent study demonstrates the importance of identifying jet coherence (or instability) on successful needle-free injections.[4] Moreover, this work is of relevance to recent advances in nanofiber production where the use of polymer solutions (which are often modeled as viscoelastic) in liquid jet stability is critical.[3] For very small diameter jets (in nanofiber productions, liquid jets have typical diameters of about 10 μm) and under high velocities, the effects of the surrounding
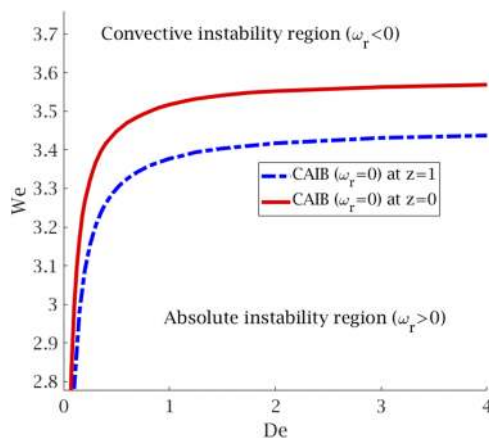

FIG. 11. Graph showing the convective/absolute instability boundary (CAIB), where We_c appears at $\omega_r = 0$, on the De–We plane, where $Re = 800$, $F = 4$, and $\alpha = 3$.

medium will become important on the resulting jet dynamics and instability. Exploring these effects will be the subject of a future paper.

ACKNOWLEDGMENTS

APPENDIX A: DIMENSIONLESS FORMS OF THE GOVERNING EQUATIONS AND THE BOUNDARY CONDITIONS

By using the nondimensional scalings, (9), the continuity equation, (3), becomes

$$\frac{\partial v_r}{\partial r} + \frac{v_r}{r} + \varepsilon \frac{\partial v_z}{\partial z} = 0. \tag{A1}$$

The radial and axial momentum equations of the Navier-Stokes equation, (4), become, respectively,

$$\varepsilon \frac{\partial v_r}{\partial t} + v_r \frac{\partial v_r}{\partial r} + \varepsilon v_z \frac{\partial v_r}{\partial z}$$
$$= -\frac{\partial p}{\partial r} + \frac{\alpha}{Re}\left(\frac{\partial^2 v_r}{\partial r^2} + \frac{1}{r}\frac{\partial v_r}{\partial r} - \frac{v_r}{r^2} + \varepsilon^2 \frac{\partial^2 v_r}{\partial z^2}\right)$$
$$+ \frac{\varepsilon}{Re}\left(\frac{\partial T_{rr}}{\partial r} + \frac{T_{rr}}{r} + \varepsilon \frac{\partial T_{zr}}{\partial z}\right), \tag{A2}$$

$$\varepsilon \frac{\partial v_z}{\partial t} + v_r \frac{\partial v_z}{\partial r} + \varepsilon v_z \frac{\partial v_z}{\partial z}$$
$$= -\varepsilon \frac{\partial p}{\partial z} + \frac{\alpha}{Re}\left(\frac{\partial^2 v_z}{\partial r^2} + \frac{1}{r}\frac{\partial v_z}{\partial r} + \varepsilon^2 \frac{\partial^2 v_z}{\partial z^2}\right)$$
$$+ \frac{\varepsilon}{Re}\left(\varepsilon \frac{\partial T_{zz}}{\partial z} + \frac{T_{rz}}{r} + \frac{\partial T_{rz}}{\partial r}\right) + \frac{1}{F^2}. \tag{A3}$$

The components of the extra stress tensor, (2), become

$$\varepsilon \frac{\partial T_{zz}}{\partial t} + v_r \frac{\partial T_{zz}}{\partial r} + \varepsilon v_z \frac{\partial T_{zz}}{\partial z} - 2T_{rz}\frac{\partial v_z}{\partial r} - 2\varepsilon T_{zz}\frac{\partial v_z}{\partial z}$$
$$= \frac{1}{De}\left(2(1-\alpha)\varepsilon \frac{\partial v_z}{\partial z} - \varepsilon T_{zz}\right), \tag{A4}$$

$$\varepsilon \frac{\partial T_{rr}}{\partial t} + v_r \frac{\partial T_{rr}}{\partial r} + \varepsilon v_z \frac{\partial T_{rr}}{\partial z} - 2T_{rr}\frac{\partial v_r}{\partial r} - 2\varepsilon T_{rz}\frac{\partial v_r}{\partial z}$$
$$= \frac{1}{De}\left(2(1-\alpha)\frac{\partial v_r}{\partial r} - \varepsilon T_{rr}\right). \tag{A5}$$

The normal stress boundary condition, (6), becomes

$$p - \frac{2\alpha}{ReE_\varepsilon^2}\left(\frac{\partial v_r}{\partial r} + \frac{\varepsilon}{2\alpha}T_{rr}\right) + \frac{2\alpha\varepsilon}{ReE_\varepsilon^2}\left(\frac{\partial \zeta}{\partial z}\right)\left(\varepsilon \frac{\partial v_r}{\partial z} + \frac{\partial v_z}{\partial r} + \frac{\varepsilon}{\alpha}T_{rz}\right)$$
$$- \frac{2\alpha\varepsilon^3}{ReE_\varepsilon^2}\left(\frac{\partial \zeta}{\partial z}\right)^2\left(\frac{\partial v_z}{\partial z} + \frac{1}{2\alpha}T_{zz}\right)$$
$$= \frac{1}{We}\left(\frac{1}{\zeta E_\varepsilon} - \frac{\varepsilon^2}{E_\varepsilon^3}\left(\frac{\partial^2 \zeta}{\partial z^2}\right)\right) \text{ at } r = \zeta_0, \tag{A6}$$

where $E_\varepsilon = \left(1 + \varepsilon^2\left(\frac{\partial \zeta}{\partial z}\right)^2\right)^{1/2}$.

The tangential stress boundary condition, (7), becomes

$$2\varepsilon\alpha\left(\frac{\partial \zeta}{\partial z}\right)\left(\frac{\partial v_r}{\partial r} - \varepsilon \frac{\partial v_z}{\partial z}\right) + \alpha\left(1 - \varepsilon^2\left(\frac{\partial \zeta}{\partial z}\right)^2\right)$$
$$\times \left(\varepsilon \frac{\partial v_r}{\partial z} + \frac{\partial v_z}{\partial r} + \varepsilon \frac{T_{rz}}{\alpha}\right) + \varepsilon^2\left(\frac{\partial \zeta}{\partial z}\right)\left(T_{rr} - T_{zz}\right) = 0 \text{ at } r = \zeta_0. \tag{A7}$$

The kinematic boundary condition, (8), becomes

$$v_r = \varepsilon\left(\frac{\partial \zeta}{\partial t} + v_z \frac{\partial \zeta}{\partial z}\right) \text{ at } r = \zeta_0. \tag{A8}$$

APPENDIX B: THE DERIVATIVE OF EQ. (13)

To illustrate the derivation of Eq. (13), we substitute the expressions (11) and (12) into our dimensionless Eqs. (A1)–(A8). After dropping the tildes for convenience, from continuity Eq. (A1), we have

$$O(1): v_{r0} = 0 \quad \text{and} \quad O(\varepsilon): v_{r1} = -\frac{1}{2}\left(\frac{\partial v_{z0}}{\partial z}\right). \tag{B1}$$

From the axial momentum equation, (A3), and using (B1), we have

$$O(1): v_{z1} = 0, \tag{B2}$$

$$O(\varepsilon): \frac{\partial v_{z0}}{\partial t} + v_{z0}\frac{\partial v_{z0}}{\partial z} = -\frac{\partial p_0}{\partial z} + \frac{\alpha}{Re}\left(4v_{z2} + \frac{\partial^2 v_{z0}}{\partial z^2}\right)$$
$$+ \frac{1}{Re}\frac{\partial T_{zz}^0}{\partial z} + \frac{1}{F^2}. \tag{B3}$$

From the tangential boundary condition, (A7), and using (B1) and (B2), we have

$$O(\varepsilon): v_{z2} = \frac{3}{2\zeta_0}\left(\frac{\partial \zeta_0}{\partial z}\right)\frac{\partial v_{z0}}{\partial z} + \frac{1}{4}\frac{\partial^2 v_{z0}}{\partial z^2}$$
$$- \frac{1}{2\alpha\zeta_0}\left(\frac{\partial \zeta_0}{\partial z}\right)(T_{rr}^0 - T_{zz}^0). \tag{B4}$$

From the normal condition, (A6), to leading order and using (B1) and (B2), we have

$$p_0 = \frac{1}{Re}\left(T_{rr}^0 - \alpha \frac{\partial v_{z0}}{\partial z}\right) + \frac{1}{We\zeta_0}. \tag{B5}$$

Substituting (B4) and (B5) into (B3) gives (13).

APPENDIX C: THE EQUATIONS RESULTING FROM THE LINEAR STABILITY ANALYSIS

Substituting (20) into our dimensionless equations (in Appendix A) leads to a system of ordinary differential equations which can be written as

$$\bar{v}_z = \frac{-1}{ik}\left(\frac{\partial \bar{v}_r}{\partial r} + \frac{\bar{v}_r}{r}\right), \tag{C1}$$

$$(\omega + ikv_{z0})\bar{v}_r = \frac{\alpha}{Re}\left(\frac{\partial^2 \bar{v}_r}{\partial r^2} + \frac{1}{r}\frac{\partial \bar{v}_r}{\partial r} - \frac{\bar{v}_r}{r^2} - k^2\bar{v}_r\right)$$
$$- \frac{\partial \bar{p}}{\partial r} + \frac{1}{Re}\left(\frac{\partial \bar{T}_{rr}}{\partial r} + \frac{\bar{T}_{rr}}{r}\right), \tag{C2}$$

$$(\omega + ikv_{z0})\bar{v}_z = -ik\bar{p} + \frac{\alpha}{Re}\left(\frac{\partial^2 \bar{v}_z}{\partial r^2} + \frac{1}{r}\frac{\partial \bar{v}_z}{\partial r} - k^2 \bar{v}_z\right)$$
$$+ \frac{1}{Re}\left(ik\bar{T}_{zz}\right), \tag{C3}$$

$$\bar{T}_{zz} = \frac{2ik}{(\omega + ikv_{z0})}\left(\frac{1}{De} + T_{zz}^0\right)\bar{v}_z, \tag{C4}$$

$$\bar{T}_{rr} = \frac{2}{(\omega + ikv_{z0})}\left(\frac{1}{De} + T_{rr}^0\right)\frac{\partial \bar{v}_r}{\partial r}, \tag{C5}$$

$$\bar{p} = \frac{1}{Re}\left(\bar{T}_{rr} + 2\alpha\frac{\partial \bar{v}_r}{\partial r}\right) + \frac{1}{We}\left(k^2 - \frac{1}{\zeta_0^2}\right)\bar{\zeta} \text{ at } r = \zeta_0, \tag{C6}$$

$$\alpha\left(ik\bar{v}_r + \frac{\partial \bar{v}_z}{\partial r}\right) + ik\bar{\zeta}\left(T_{rr}^0 - T_{zz}^0\right) = 0 \text{ at } r = \zeta_0, \tag{C7}$$

$$\bar{\zeta} = \frac{\bar{v}_r}{(\omega + ikv_{z0})} \text{ at } r = \zeta_0. \tag{C8}$$

REFERENCES

[1] K. Kupfer, A. Bers, and A. Ram, "The cusp map in the complex-frequency plane for absolute instabilities," Phys. Fluids **30**, 3075–3082 (1987).

[2] Z. Du, X. Yu, and Y. Han, "Inkjet printing of viscoelastic polymer inks," Chin. Chem. Lett. **29**, 399–404 (2018).

[3] S. Gadkari, "Influence of polymer relaxation time on the electrospinning process: Numerical investigation," Polymers **9**, 501 (2017).

[4] M. Moradiafrapoli and J. Marston, "High-speed video investigation of jet dynamics from narrow orifices for needle-free injection," Chem. Eng. Res. Des. **117**, 110–121 (2017).

[5] J. Eggers and E. Villermaux, "Physics of liquid jets," Rep. Prog. Phys. **71**, 036601 (2008).

[6] M. F. Afzaal, J. Uddin, A. M. Alsharif, and M. Mohsin, "Temporal and spatial instability of a compound jet in a surrounding gas," Phys. Fluids **27**, 044106 (2015).

[7] R. Bassi, "Absolute instability in curved liquid jets," Ph.D. thesis, University of Birmingham, 2011.

[8] F. Suñol and R. González-Cinca, "Liquid jet breakup and subsequent droplet dynamics under normal gravity and in microgravity conditions," Phys. Fluids **27**, 077102 (2015).

[9] Lord Rayleigh, "On the instability of jets," Proc. London Math. Soc. **s1**, 4–13 (1878).

[10] C. Weber, "Zum zerfall eines flüssigkeitsstrahles," Z. Angew. Math. Mech. **11**, 136–154 (1931).

[11] S. Middleman, "Stability of a viscoelastic jet," Chem. Eng. Sci. **20**, 1037–1040 (1965).

[12] M. Goldin, J. Yerushalmi, R. Pfeffer, and R. Shinnar, "Breakup of a laminar capillary jet of a viscoelastic fluid," J. Fluid Mech. **38**, 689–711 (1969).

[13] D. T. Papageorgiou, "On the breakup of viscous liquid threads," Phys. Fluids **7**, 1529–1544 (1995).

[14] B. Cheong and T. Howes, "Capillary jet instability under the influence of gravity," Chem. Eng. Sci. **59**, 2145–2157 (2004).

[15] U. S. Sauter and H. W. Buggisch, "Stability of initially slow viscous jets driven by gravity," J. Fluid Mech. **533**, 237–257 (2005).

[16] A. M. Alsharif, "Instability of non-uniform viscoelastic liquid jets," Ph.D. thesis, University of Birmingham, 2014.

[17] H.-Y. Ye, L.-J. Yang, and Q.-F. Fu, "Instability of viscoelastic compound jets," Phys. Fluids **28**, 043101 (2016).

[18] S. Leib and M. Goldstein, "The generation of capillary instabilities on a liquid jet," J. Fluid Mech. **168**, 479–500 (1986).

[19] S. Leib and M. Goldstein, "Convective and absolute instability of a viscous liquid jet," Phys. Fluids **29**, 952–954 (1986).

[20] R. J. Briggs, *Electron-Stream Interaction with Plasmas* (MIT Press, Monograph MIT, Cambridge USA, 1964).

[21] S. Lin and Z. Lian, "Absolute instability of a liquid jet in a gas," Phys. Fluids A **1**, 490–493 (1989).

[22] B. O'Donnell, J. Chen, and S. Lin, "Transition from convective to absolute instability in a liquid jet," Phys. Fluids **13**, 2732–2734 (2001).

[23] S. Lin and E. Ibrahim, "Instability of a viscous liquid jet surrounded by a viscous gas in a vertical pipe," J. Fluid Mech. **218**, 641–658 (1990).

[24] G. Amini and M. Ihme, "Liquid jet instability under gravity effects," in *51st AIAA Aerospace Sciences Meeting including the New Horizons Forum and Aerospace Exposition* (AIAA, 2013), p. 92.

[25] L.-J. Yang, M.-X. Tong, and Q.-F. Fu, "Linear stability analysis of a three-dimensional viscoelastic liquid jet surrounded by a swirling air stream," J. Non-Newtonian Fluid Mech. **191**, 1–13 (2013).

[26] R. B. Bird, R. C. Armstrong, and O. Hassager, *Dynamics of Polymeric Liquids*, Fluid Mechanics, Vol. 1 (Wiley, 1987).

[27] F. Li, X.-Y. Yin, and X.-Z. Yin, "Axisymmetric and non-axisymmetric instability of an electrically charged viscoelastic liquid jet," J. Non-Newtonian Fluid Mech. **166**, 1024–1032 (2011).

[28] J. N. Anno, *The Mechanics of Liquid Jets* (D. C. Heath, Lexington, MA, 1977), p. 118.

[29] M. Verhoef, B. van den Brule, and M. Hulsen, "On the modelling of a PIB/PB Boger fluid in extensional flow," J. Non-Newtonian Fluid Mech. **80**, 155–182 (1999).

[30] R. B. Bird, R. C. Armstrong, O. Hassager, and C. F. Curtiss, *Dynamics of Polymeric Liquids* (Wiley, New York, 1977), Vol. 1.

[31] J. Eggers, "Nonlinear dynamics and breakup of free-surface flows," Rev. Mod. Phys. **69**, 865 (1997).

[32] J. Uddin, "An investigation into methods to control breakup and droplet formation in single and compound liquid jets," Ph.D. thesis, University of Birmingham, Birmingham, UK, 2007.

[33] C. Clasen, J. Eggers, M. A. Fontelos, J. Li, and G. H. McKinley, "The beads-on-string structure of viscoelastic threads," J. Fluid Mech. **556**, 283–308 (2006).

[34] D. Deshawar and P. Chokshi, "Stability analysis of an electrospinning jet of polymeric fluids," Polymer **131**, 34–49 (2017).

[35] D. N. Riahi, K. Lozano, L. Cremar, and A. Fuentes, "On nonlinear rotating polymeric jets during forcespinning process," Fluid Dyn. Res. **50**, 065507 (2018).

[36] S. Nonnenmacher and M. Piesche, "Stability behavior of liquid jets under gravity," Chem. Eng. Technol. **27**, 529–536 (2004).

[37] G. Brenn, Z. Liu, and F. Durst, "Linear analysis of the temporal instability of axisymmetrical non-Newtonian liquid jets," Int. J. Multiphase Flow **26**, 1621–1644 (2000).

[38] A.-C. Ruo, F. Chen, C.-A. Chung, and M.-H. Chang, "Three-dimensional response of unrelaxed tension to instability of viscoelastic jets," J. Fluid Mech. **682**, 558–576 (2011).

[39] J. B. Keller, S. Rubinow, and Y. Tu, "Spatial instability of a jet," Phys. Fluids **16**, 2052–2055 (1973).

[40] D. Busker, A. Lamers, and J. Nieuwenhuizen, "The non-linear break-up of an inviscid liquid jet using the spatial-instability method," Chem. Eng. Sci. **44**, 377–386 (1989).

[41] T. Si, F. Li, X.-Y. Yin, and X.-Z. Yin, "Modes in flow focusing and instability of coaxial liquid–gas jets," J. Fluid Mech. **629**, 1–23 (2009).

[42] L. Xie, L.-j. Yang, L.-z. Qin, and Q.-f. Fu, "Temporal instability of charged viscoelastic liquid jets under an axial electric field," Eur. J. Mech.: B/Fluids **66**, 60–70 (2017).

[43] P. G. Drazin and W. H. Reid, *Hydrodynamic Stability* (Cambridge University Press, 1981).

[44] P. K. Ray and T. A. Zaki, "Absolute/convective instability of planar viscoelastic jets," Phys. Fluids **27**, 014110 (2015).

[45] F. Li, B.-F. Wang, Z.-H. Wan, J. Wu, and M. Zhang, "Absolute and convective instabilities in electrohydrodynamic flow subjected to a Poiseuille flow: A linear analysis," J. Fluid Mech. **862**, 816–844 (2019).

[46] R. Patne and V. Shankar, "Absolute and convective instabilities in combined Couette-Poiseuille flow past a neo-Hookean solid," Phys. Fluids **29**, 124104 (2017).

[47]C. Camporeale, R. Vesipa, and L. Ridolfi, "Convective-absolute nature of ripple instabilities on ice and icicles," Phys. Rev. Fluids **2**, 053904 (2017).

[48]G. Balestra, M. Gloor, and L. Kleiser, "Absolute and convective instabilities of heated coaxial jet flow," Phys. Fluids **27**, 054101 (2015).

[49]R. Vesipa, C. Camporeale, L. Ridolfi, and J. M. Chomaz, "On the convective-absolute nature of river bedform instabilities," Phys. Fluids **26**, 124104 (2014).

[50]A. S. Mohamed, M. Herrada, A. Gañán-Calvo, and J. Montanero, "Convective-to-absolute instability transition in a viscoelastic capillary jet subject to unrelaxed axial elastic tension," Phys. Rev. E **92**, 023006 (2015).

[51]F. Li, A. M. Gañán-Calvo, and J. M. López-Herrera, "Absolute-convective instability transition of low permittivity, low conductivity charged viscous liquid jets under axial electric fields," Phys. Fluids **23**, 094108 (2011).

[52]S. Lin and Z. Lian, "Absolute and convective instability of a viscous liquid jet surrounded by a viscous gas in a vertical pipe," Phys. Fluids A **5**, 771–773 (1993).

[53]J. M. López-Herrera, A. M. Gañán-Calvo, and M. A. Herrada, "Absolute to convective instability transition in charged liquid jets," Phys. Fluids **22**, 062002 (2010).